High spatial resolution imaging of subcellular macro and trace element distribution during phagocytosis

Maria Angels Subirana, Sina Riemschneider, Gerd Hause, Dirk Dobritzsch, Dirk Schaumlöffel, Martin Herzberg

High spatial resolution imaging of subcellular macro and trace element distribution during phagocytosis

Maria Angels Subirana[a], Sina Riemschneider[b], Gerd Hause[c], Dirk Dobritzsch[d], Dirk Schaumlöffel[a,e*] and Martin Herzberg[f]

[a] CNRS, Université de Pau et des Pays de l'Adour, E2S UPPA, Institut des Sciences Analytiques et de Physico-Chimie pour l'Environnement et les Matériaux (IPREM), UMR 5254, 64000 Pau, France

[b] Fraunhofer Institute for Cell Therapy and Immunology (IZI), 04103 Leipzig, Germany

[c] Martin-Luther-University Halle-Wittenberg, Biozentrum, Weinbergweg 22, 06120 Halle (Saale), Germany

[d] Martin-Luther-University Halle-Wittenberg, Core Facility – Proteomic Mass Spectrometry, Kurt-Mothes-Str. 3a, 06120 Halle (Saale), Germany

[e] Peoples' Friendship University of Russia (RUDN University), Mklukho-Maklaya str. 6, 117198 Moscow, Russia

[f]Martin-Luther-University Halle-Wittenberg, Institute for Biology / Microbiology, Kurt-Mothes-Str. 3, 06120 Halle/Saale, Germany

*Correspondence should be addressed to Dirk Schaumlöffel; dirk.schaumloeffel@univ-pau.fr

Short running head: Subcellular element distribution during phagocytosis

Keywords: NanoSIMS, ICP-MS, Trace elements, mass spectrometry, macrophage, *Salmonella*

Significance to metallomics

Analyses of the composition of the cellular metallome and the spatial resolution of elemental distribution within the cell are key information for a better understanding of cellular processes. Besides a large number of biochemical reactions catalyzed by trace elements as part of the metalloproteome of a cell, these metals play a central role during phagocytosis, the main player of the cellular immune response. Using a combination of quantitative (ICP-MS) and spatially resolved mass spectrometry (NanoSIMS) in combination with optical spectroscopy and Transmission Electron Microscopy (TEM), this work describes the distribution of macro- and trace elements during phagocytosis, using murine macrophages and Salmonella as model system.

Abstract

The bioavailability of trace elements in the course of evolution had an essential influence on the emergence of life itself. This is reflected in the co-evolution between eukaryotes and prokaryotes. In this study, the influence and cellular distribution of bioelements during phagocytosis at the host-pathogen interface was investigated using high-resolution nanoscale secondary ion mass spectrometry (NanoSIMS) and quantitative inductively coupled plasma mass spectrometry (ICP-MS). In the eukaryotic murine macrophages (RAW 264.7 cell line), the cellular Fe / Zn ratio was found to be balanced, whereas the dominance of iron in the prokaryotic cells of the pathogen *Salmonella enterica* Serovar Enteritidis was about 90% compared to zinc. This confirms the evolutionary increased zinc requirement of the eukaryotic animal cell. Using NanoSIMS, the Cs^+ primary ion source allowed high spatial resolution mapping of cell morphology down to subcellular level. At a comparable resolution, several low abundant trace elements could be mapped during phagocytosis with a RF plasma O^- primary ion source. An enrichment of copper and nickel could be detected in the prokaryotic cells.

Surprisingly, an accumulation of cobalt in the area of nuclear envelope was observed indicating an interesting but still unknown distribution of this trace element in murine macrophages.

Graphical Abstract

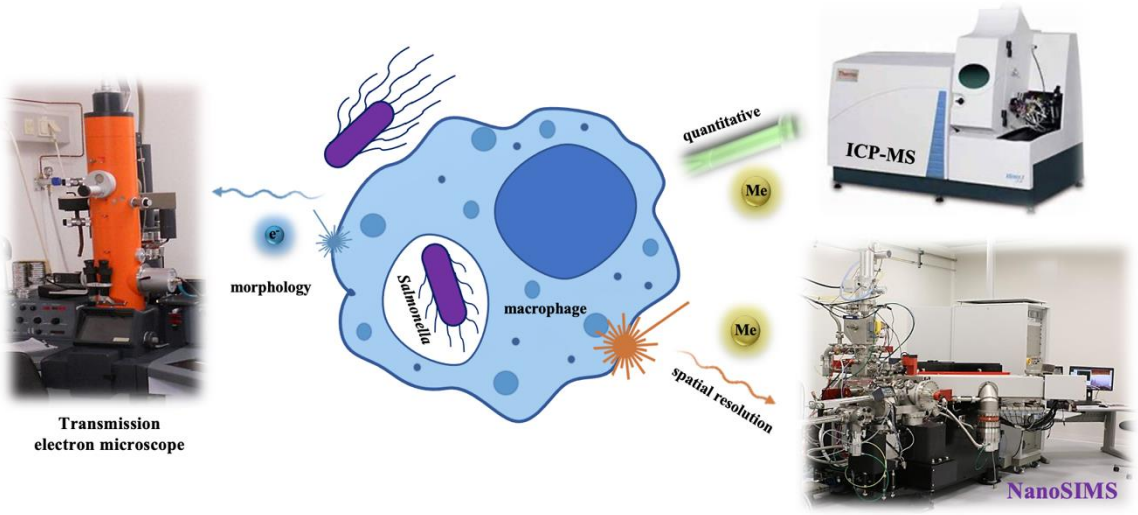

Introduction

Macrophages are key players in innate immunity and the cellular functions of phagocytosis play a central role in the defense against pathogens by cells of the eukaryotic innate immune system at the host-pathogen interface. The occurrence of phagocytotic active cells is not limited to the immune system, but arose early in evolution before the advent of multicellularity [1-5]. The phagocytosis processes of predatory protozoan and their bacteria prey have evolved for the last 2 billion years [6]. There are remarkable similarities to mammalian macrophages, one being the major challenge for bacteria to obtain sufficient metal ions for growth in the host environment [7]. The role of iron and manganese sequestration is assumed and the intoxication by zinc and copper as an antimicrobial strategy is a rising hypothesis within the last decade [8]. Thus, antimicrobial host actions, and the corresponding bacterial defenses have a long evolutionary history [9]. Bioavailability of trace metals regulates host-pathogen as well as predator-prey interactions during phagocytosis [10]. In case of host-pathogen relation, the cytoplasm of the host provides the source of metals and changes the metal composition and trafficking after pathogen detection. It has been shown that iron and manganese from the pathogenic vacuole (phagosome) is retained, but the changes in copper and zinc pools are still under discussion. Several mammalian infection studies have focused on the effects of metal deficiency and overloading or poising at the cellular and subcellular level [7, 11-13].

Element-specific imaging enables the localization of chemical elements including trace metals in biological tissue and cells and, hence, has the potential to investigate biochemical functions, biosorption and bioaccumulation processes of trace elements at the cellular and even at the subcellular level [14]. Nanoscale secondary ion mass spectrometry (NanoSIMS) is a technique where a primary ion beam sputters the surface of a sample and the resulting secondary ions are separated and detected in a mass spectrometer [15]. However, the limitation is the generation of ions from the sample, that depend on the atomic density of the analyte in the surface, the

sputtering rate (the rate of ejection of the analyte from the surface by the primary ions) and the ionization yield (the fraction of sputtered atoms that are ionized) [16]. The ionization yield depends, in turn, on the ionization energy for positive secondary ions and the electron affinity for negative ions [17]. Either a cesium (Cs^+) or oxygen (O^-) primary ion beam scans the sample surface and thus produce elemental maps with a resolution down to 50 nm. A cesium ion source is well established to generate and map negative secondary ions (e.g., C^-, CN^-, O^-, and P^-) in biological samples. In the meantime, the recent implementation of a bright RF plasma O^- primary ion source in NanoSIMS for the generation of positive secondary ions [18] (e.g., Na^+, Ca^+, Fe^+, Co^+, Ni^+, and Cu^+) allows the mapping of trace metals in cells with similar spatial resolution than the cesium source, down to 40 nm, and paves the way for metal detection inside bacteria.

Up to now, all NanoSIMS studies on bacteria employed the cesium ion source mainly for the investigation of metabolic activities using stable isotopes such as ^{13}C and ^{15}N [19, 20]. Even in those few studies where bacteria metabolisms of metal ions were regarded, the metals themselves were rarely analyzed by NanoSIMS. The exceptional cases in which NanoSIMS was used are limited to those metals whose oxide ions can be generated by the Cs^+ source. For example, to investigate radionuclide uptake by bacteria $^{238}U^{16}O^-$ was detected simultaneously with $^{13}C^{14}N^-$ to show uraninite (UO_2) nanocrystal precipitation on the surface of *G. sulfurreducens* cells [21]. The same bacteria were used to study microbial iron reduction where iron was detected as $^{56}Fe^{16}O^-$ on the substrate surface, but not in the bacteria itself [22]. A similar approach was used to investigate the Fe-oxidizing bacterium *Leptothrix ochracea* [23, 24]. In addition, NanoSIMS was employed to observe aluminum and copper (via $^{27}Al^{16}O^-$ and $^{63}Cu^{16}O^-$ secondary ions) in bacteria induced biominerals [25]. A recent work studied arsenic reduction in presence of iron by the *Shewanella* bacterium via subcellular detection of $^{56}Fe^{12}C^-$, $^{56}Fe^{16}O^-$, and $^{75}As^-$ [26]. Furthermore, the bioimaging of macrophages with

NanoSIMS is limited to few studies too. Again, mainly the stable isotopes ^{13}C and ^{15}N together with the cesium ion source were employed to explore cholesterol metabolism [27, 28] or the intracellular localization of drugs [29-31] in macrophages.

Few publications describe metal imaging in macrophages by synchrotron radiation X-ray fluorescence (SXRF), which is a complementary technique to NanoSIMS for elemental mapping in biological samples. Although recent developments have allowed the optimization of some beamlines to achieve spatial resolutions similar to NanoSIMS, macrophage analyses were reported with spatial resolution at the low micrometer level, which provided rather diffuse images and did not allow metal localization at the organelle level. An early work of Kitamura and coworkers showed the local distribution of chromium, iron, zinc, and calcium in single macrophage cell at 5 µm resolution [32, 33]. With the same resolution, mercury, selenium, zinc and copper accumulation was observed in macrophage aggregates of yelloweye rockfish liver [34]. The phagocytosis of asbestos fibers was visualized by the SXRF mapping of calcium, magnesium, iron, and silicon in macrophages with a beam size of 0.2 µm × 1 µm [35]. In a similar study, iron release from carbon nanotubes was observed in in murine macrophages with a beam size of 0.4 µm × 0.9 µm [36]. To our knowledge, no study investigated so far intracellular metal distribution in macrophages and bacteria during phagocytosis due to the lack of both high-sensitive and high-resolution imaging techniques for trace elements.

We report here for the first time high-sensitive and high-resolution imaging of macro and trace elements at cellular and subcellular level in macrophages and bacteria using NanoSIMS equipped with a bright RF plasma O^- primary ion source as well as a conventional cesium ion source. The aim was to visualize the elemental distribution and accumulation of metals during phagocytosis of bacteria. The model system was the murine RAW 264.7 macrophage cell line in combination with the pathogen *Salmonella enterica* Serovar Enteritidis (*Sa*). This model system is well established and has been used for decades to study phagocytosis [37-40].

Employing both ion sources in NanoSIMS, non-metals (C, N, P, S) as well as metal (Na and Ca) macroelements and trace metals (Mn, Fe, Co, Ni, Cu,) can be analyzed and associated to subcellular structures allowing the discussion of the biological role and cellular distribution of these elements during phagocytosis.

Material and Methods

Bacterial strain and growth conditions

Salmonella enterica Serovar Enteritidis (*Sa*) was cultivated in complex medium LB (Difco™ LB Broth, Lennox). Cultures were shaken aerobically at 37 °C. A first pre-culture was incubated for 16 h, and diluted 1 to 400 and incubated for 2 h (second pre-culture), which was then used to inoculate the main culture, also at a dilution of 1 to 400. This allowed highly reproducible steady-state growth to the mid-exponential phase. Samples from culture were used to determine the colony-forming units (cfu) as a function of cell number.

Cell culture of murine macrophage cell line RAW 264.7

RAW 264.7 (ATCC® TIB-71™) represents a murine (BALB/c; $H2^d$) adherent growing monocyte/macrophage cell line which is transformed by Abelson murine leukemia virus. RAW 264.7 cells are capable of pinocytosis and phagocytosis, antibody-dependent lysis of tumor cells as well as nitric oxide (NO) and cytokine production and they are responsive to LPS. Cells were cultured in 175 cm^2 cell culture flasks (Greiner Bio-One, Frickenhausen, Germany) in phenol-red free RPMI 1640 medium supplemented with 10 % FBS, 2 mM L-glutamine, 10 mM HEPES buffer, 100 µg/ml penicillin/streptomycin (Biochrom, Berlin, Germany) and 50 µM β-mercaptoethanol (Sigma Aldrich, Steinheim, Germany) at 37 °C, 5% CO_2 and 95% air humidity. Cell numbers were determined by cell counting chamber.

Determination of metal content by means of inductively coupled plasma - mass spectrometry analysis (ICP-MS)

To determine the metal content, *Sa* were cultivated until mid-exponential phase of growth. A 10 mL cell suspension was centrifuged for 30 min at 4 °C and at 4,500 × g. Cells were washed twice with 50 mM Tris-HCl buffer containing 10 mM EDTA (pH 7). The supernatant was discarded and the residual liquid carefully removed at each step. RAW 264.7 cells were cultured at a density of 1×10^6 cells / ml in 58 cm^2 cell culture dishes with 10 ml of cell culture medium

described above. Afterwards RAW 264.7 cells were incubated and stimulated with 1×10^8 heat inactivated *Sa* (hi*Sa*; inactivation by 60 °C for 1 h) or not as control. After 4 h cells were harvested and washed twice with Phosphate-buffered saline (0.15 M NaCl, pH 7.4; PBS) containing 5 mM EDTA (Sigma Aldrich). The pellet was suspended in concentrated 67% (w/v) HNO_3 (trace metal grade; BDH Prolabo®, VWR, Darmstadt, Germany) and mineralized at 70 °C for 2 h. Samples were diluted to a final concentration of 2% (w/v) nitric acid. Indium was added as internal standard at a final concentration of 10 ppb. Elemental analysis was performed via inductively coupled plasma mass spectrometry (ICP-MS) using ESI-sampler SC-2 (Elemental Scientific Inc., Omaha, USA) and an X-Series II ICP-MS instrument (Thermo Fisher Scientific, Bremen, Germany) operating with a collision/reaction cell and flow rates of 5 ml/min of He/H_2 (93% / 7%), with an Ar carrier flow rate of 0.76 L/min and an Ar make-up flow rate of 15 l/min. An external calibration curve was recorded with ICP-multi element standard solution XVI (Merck, Darmstadt, Germany) in 2% nitric acid. Each sample was introduced via a peristaltic pump and analyzed for its metal content. For blank measurement and quality/quantity thresholds, calculations were performed based on DIN32645 (this standard procedure describes in chemical analysis - decision limit, detection limit and determination limit under repeatability conditions - terms, methods, evaluation; ICS Code – 71.040.01). The results were transformed from concentrations via molar units into atoms per sample and divided by the number of cells per sample.

Phagocytosis assay with macrophages RAW 264.7 and FITC-labelled Sa

Firstly, 1×10^9 heat inactivated *Sa* were incubated with 0.20 mg Fluorescein isothiocyanate (FITC) in 2.0 mL carbonate buffer (0.10 M) for 1 h protected from light. After incubation the *Sa* were centrifuged and washed for five times with PBS. For phagocytosis assay 4×10^7 FITC-labelled heat inactivated *Sa* were incubated with 1×10^6 RAW 264.7 for 40 min at 37 °C in cell culture medium. Afterwards the cells were plated onto a microscope slide via cytocentrifuge

Shandon Cytospin (Thermo, Germany). Pictures were taken with phase contrast and fluorescence microscopy by Primovert (Zeiss, Germany).

Sample preparation of macrophages and Sa for transmission electron microscopy and NanoSIMS

1×10^7 RAW 264.7 cells were co-cultured with 1×10^4 *Sa* for 15 h in RPMI medium. After cultivation the cells were fixed directly with 3% glutaraldehyde (Sigma, Taufkirchen, Germany) in 0.10 M sodium cacodylate buffer (SCB) for 3 h, centrifuged at 5000 rpm for 5 min and taken up in 4% agar/SCB, followed by one wash-step with SCB-buffer overnight at 4 °C and three wash-steps with the same buffer for 5 min. For TEM analysis the samples were postfixed with 1% osmium (VIII) tetroxide in SCB for 1 h. After washing with H_2O samples were dehydrated in a series of ethanol (2 times for 5 min. with 25%, 50%, 75% and 100% ethanol each). Thereafter the samples were infiltrated with epoxy resin according to Spurr [41] and polymerized at 70 °C. Subsequent ultrathin sections of 80 nm and 300 nm were cut with an Ultracut R ultramicrotome (Leica, Wetzlar, Germany). The 80 nm ultrathin sections were placed on copper grids and observed with an EM900 transmission electron microscope (Carl Zeiss Microscopy, Oberkochen, Germany) operating at 80 kV. The images were recorded using a Variospeed SSCCD camera SM-1k-120 (TRS, Moorenweis, Germany). The 300 nm sections were placed on silicon wafers for NanoSIMS analysis.

NanoSIMS analysis

Elemental distribution of non-metals, micronutrients and trace metals was analyzed on the ultrathin sections with a NanoSIMS 50L (Cameca, Gennevilliers, France), equipped with seven parallel electron multiplier detectors. A Cs^+ ion source was used for the mapping of carbon ($^{12}C_2^-$), nitrogen ($^{12}C^{14}N^-$), sulfur ($^{32}S^-$), and phosphorus ($^{31}P^-$) in selected macrophage cells, with a current of approximately 0.25 pA. Areas between 20 µm × 20 µm and 30 µm × 30 µm were pre-sputtered (10 min at 100 pA, for cesium implantation in order to increase the

secondary ion yield) and subsequently analyzed with 512 × 512 pixels, and a dwell time of 10 ms per pixel. Afterwards, regions of interest between 2 µm × 2 µm and 3 µm × 3 µm were analyzed in detail with 128 × 128 pixels and the same dwell time.

A Hyperion^{TM} RF plasma O^- ion source [18] was used to map sodium ($^{23}Na^+$), potassium ($^{39}K^+$), calcium ($^{40}Ca^+$), manganese ($^{55}Mn^+$), iron ($^{56}Fe^+$), nickel ($^{58}Ni^+$), cobalt ($^{59}Co^+$) and copper ($^{63}Cu^+$). For these isotopes, the electron multiplier detectors cannot be placed at mass differences of only 1 amu (atomic mass unit). Therefore, two different mass calibrations were necessary, one for the analysis of C, Na, Ca, Fe and Co and another for C, Na, K, Mn, Ni and Cu. Areas between 20 µm × 20 µm and 65 µm × 65 µm were analyzed with 256 × 256 pixels, 10 ms dwell time and a current of 5 pA. Later, regions of interest of approx. between 5 µm × 5 µm and 25 µm × 25 µm were mapped with a beam of 1.5 pA for the detection of the macronutrients Na, Ca, and K, and then the same regions were mapped with 25 pA for trace metal detection.

Mass calibration was performed with element standards obtained from standard solutions (PlasmaCAL, SPC Science, Canada) dropped and evaporated on silicon wafers. Mass resolution was optimized to resolve possible interferences, but entrance and aperture slits were open to allow maximum transmission of the ions of the trace elements, which resulted in a mass resolution of approximately 3000-5000. The cluster ion $^{12}C^{14}N^-$ was detected to maximize the signal measured for ^{14}N, and mapping of ^{12}C, originating from the resin, was used to control homogeneous sputtering of the area. Image processing was performed using the software WinImage (Cameca). Several maps of the same area were acquired and stacked to obtain the final image. The diameter of the primary ion beam (probe size) determining the spatial resolution was measured and calculated by the knife-edge method (16-84% criterion) [18] in several points of an image and an average was given. An example is presented in Supplementary Figure 1.

Results and Discussion

Cellular metal content of *S. enterica* Serovar Enteritidis and murine macrophages

The element composition in a cell and the relationship to cellular and subcellular distribution for cell biology functions, are key factors for understanding biochemical processes in cells and multicellular organisms. A quantitative analysis of the cellular metal content, also known as metallome or metal quota, in *Sa* and murine macrophage cell line RAW 264.7 was done by ICP-MS. In both organisms, the macroelement magnesium (Mg) dominates the metal content, surpassing the following most abundant metals calcium (Ca), iron (Fe) and zinc (Zn), by approximately one order of magnitude (Figure 1, Supplementary Table 1). The amounts of these elements found in both organisms are in agreement with their occurrence as metal co-factors of enzymes shown in recent database analyses, where Mg was found to be in 16% of enzymes, Zn in 9%, Fe in 8%, Mn in 6% and Ca in 2% [42, 43]. In comparison, other trace metals such as Cu, Co, Ni and molybdenum (Mo) are present in much lower amounts (Supplementary Table 1), as they are also used in less enzymatic processes [42, 43]. All these metals are essential co-factors in enzymatic reactions or have structural functions in metalloproteins. Manganese (Mn), for example, is an essential element for most living organisms and has several biochemical functions as an integral component of enzymes like pyruvate carboxylases, arginases and superoxide dismutases, while several other enzymes, including kinases, transferases, hydrolyses and decarboxylases can be activated by manganese [44, 45]. Copper (Cu) is often employed by metal binding enzymes to catalyze electron transfer for energy production and by superoxide dismutase to perform an antioxidant activity [46-50]. As metal co-factor nickel is found in enzymes like NiFe-hydrogenases and ureases of archaea, bacteria, plants, and primitive eukaryotes [51]. Cobalt (Co) has its primary role in cobalamin as a co-factor of individual enzymes, methylmalonyl-CoA mutase, methionine synthase and methionyl aminopeptidase [48-50]. In order to gain biological activity and function in enzymes, Mo is

complexed with pterin, with the exception of the bacterial Mo-nitrogenase, and can be found in small amounts in eukaryotes and prokaryotes [52, 53].

Beside Mg, the trace metals zinc and iron are the two most abundant cofactors in proteomes (metalloproteomes) with a variety of biological and biochemical functions [54]. The high cellular iron content determined here in *Sa* and murine macrophages (Figure 1) is explained by its use in the active centers of hundreds of enzymes and in oxygen carrier proteins [55, 56]. Furthermore, iron can be bound by glutathione and stored cellularly by ferritin or bacterioferritin in prokaryotes and eukaryotes [56-59]. Iron plays a critical role in energy conservation during electron transfer in the respiratory chain as a component of cytochromes and cytochrome oxidase, coordinated in heme or iron sulfur (2Fe-2S / 4Fe-4S) complexes [60]. Furthermore, redox-active iron gains importance as a cofactor of various enzymes in a multitude of metabolic pathways, such as in ribonucleotide reductases for DNA synthesis or in the TCA cycle in succinate dehydrogenases and aconitases.

In the case of zinc (Figure 1), this element is redox-inactive, but it is also a structural and catalytic key component of hundreds of proteins and is involved in all levels of cellular signal transduction and regulation. Besides, it has significant functions in cell growth, development, transcription, cell division, oxidative stress, apoptosis and aging [61, 62]. Bioinformatic analyses suggest that iron and zinc proteins represent about 10 % of the prokaryotic and eukaryotic proteomes [63, 64].

The determination of the cellular ratio of these two elements shows that the iron quota in *Sa* dominates compared to zinc with 91 % to 6 % in the metal pool. In eukaryotic cells, here the murine macrophages, this ratio shifts towards zinc with a percentage of 53 % iron to 43 % zinc (Figure 1 C & D). Previously studies have shown that the Zn/Fe ratio shifts in the metallomes between prokaryotic and eukaryotic cells, primarily with the recruitment of metal co-factors used in the metalloproteome [63-67]. Further bioinformatic comparisons of coding protein-

metal binding motifs between eukaryotes and prokaryotes predict that eukaryotic metalloproteomes require more zinc and less iron due to a higher content of zinc binding proteins, especially by the high number of zinc finger proteins in regulatory processes. [68-70]. In addition, eukaryotic organisms are able to store and accumulate zinc in subcellular compartments, whereas prokaryotes cannot. However, both eukaryotes and prokaryotes have storage and buffering capabilities in the form of metallothioneins and metal binding stretches in P-loop GTPases as well as ribosomes as zinc sink [71-78].

Exceptions to the dominating abundance of magnesium, iron and zinc can be seen by the rising abundance of single elements, such as calcium, through strong metal fluxes in form of regulation as a second messenger. The functions of calcium ions (Ca^{2+}) in cell signaling processes as universal messenger in eukaryotes and in regulation of gene expression as well as regulation of intracellular processes have been studied for a long time [79-81]. However, the physiological role in prokaryotic cells remains unclear and is still unexplored [82]. Only indirect evidence shows that Ca^{2+} affects several bacterial physiological processes [83-85]. Similar to eukaryotes, bacteria maintain the cytosol free of Ca^{2+} within the nanomolar range even in the presence of mM extracellular concentration [82, 86-90]. This different range of functions in eukaryotes and prokaryotes is reflected in the quantitative determination of cellular calcium content between the organisms shown here, with an order of magnitude higher percentage of calcium in macrophages than in *Salmonella*, compared to the ratio of the other determined cellular metal contents (Figure 1, Supplementary Table 1).

Morphology & cell biology imaging

Macrophages play a major role in the immune response to most infections along with other professional phagocytes like neutrophils and monocytes or non-professional dendritic cells [91]. The process of phagocytosis is a type of endocytosis, first noticed by William Osler [92]

and studied and named by Élie Metchnikoff [93, 94]. It is described as “the ingestion of solid particulate matter by cells” [95]. Enveloping of the plasma membrane results in the engulfing of large particles (≥ 0.5 µm) like bacteria or other pathogens, giving rise to an internal compartment called the phagosome (Figure 2). Macrophages discriminate between infectious agents and self or other body's own cells by conserved pathogen-associated molecular patterns (PAMPs) presented on the pathogen cell surface, such as lipopolysaccharides or lipoteichoic acids of *Sa*, which can be recognized by phagocytotic receptors, like membrane-bound Dectin-1, mannose receptors, CD14 and scavenger receptor A (SR-A) [96, 97]. These molecular and cell biological processes are shown in Figure 2 (A) as a live cell image during the process of phagocytosis. The heat inactivated FITC-labelled *Sa* are represented by green fluorescence. The bacteria (*Sa*) are located outside and inside the macrophages. Figure 2 (B) shows a light microscope image of an 1 µm semi-thin section stained with toluidine blue after fixation and epoxy resin embedding of after 15 h of incubation of macrophages and *Sa*. Cell shape and nucleus as well as possibly enclosed bacteria in vesicular structures become visible in the light microscopic resolution as an overview image. Using transmission electron microscopy, in the control with heat inactivated *Sa* incubation (Figure 2 (C)) subcellular structures such as vesicles of different sizes, mitochondria, nucleus, nucleolus and nuclear envelope, also known as nuclear membrane, can be identified. In Figure 2 (D), after incubation with intact *Sa*, these bacterial structures can be shown in vesicles corresponding to the phagosomes or phagolysosomes.

NanoSIMS analysis

Further investigation of the elemental distribution and partitioning of the metallome between eukaryote and prokaryote cells was performed qualitatively by NanoSIMS. From the elements that were quantified by ICP-MS, a selection was made for NanoSIMS analyses, based on their relevance and their relative sensitivity. Please note that NanoSIMS shows different sensitivity

to different elements, thus it is only semi-quantitative allowing the measurement of the relative distribution of an element in an image but not a quantitative comparison between elements as it is possible by ICP-MS. Furthermore, quantitative elemental imaging by NanoSIMS is limited due to the sample preparation by chemical fixation and resin embedding since a leach of elements and the occurrence of artifacts can never be completely excluded.

Concerning non-metals, phosphorus (P) is contained in every living cell and is found at an order of magnitude higher in quantity than magnesium, while the basic elements C, N and O are the main constituents [98, 99]. As a structural component of cell membranes and nucleic acids, phosphorus is involved in many biological processes [100, 101]. Sulfur occurs as the fifth major non-metal element in all the major classes of biomolecules [99]. Sulfur can be found in a lower but close stoichiometry to P compared with C and N (C:N:P:S – 42:6:1:0.4) in cells [102-104]. For NanoSIMS detection, N has a low negative ion yield, but is able to form a molecular species with C, as $^{12}C^{14}N^-$, which produces a high yield [105]. Thus, the use of the Cs^+ source, with the production of high-count rates by non-metal macroelements, as $^{12}C^{14}N^-$, $^{31}P^-$ and $^{32}S^-$ ions, leads to a high-resolution cell structure and shape imaging of eukaryotic cells and subcellular structures as well as bacterial cells (Figure 3 and Supplementary Figure 2). The small current beam of 0.25 pA, enables to attain spatial resolution between 100 nm and 130 nm. Vesicles such as endosomes and phagosomes appear as empty spaces in the macrophage cell due to the leaching processes during sample preparation (Figure 3 A_1). Increased subcellular nitrogen and phosphorus concentrations show the nuclear envelope and the nucleolus in the imaging (Figure 3 A_1, A_2 & C_1, C_2). This elemental concentration can be caused by chromosome condensation of the heterochromatin at the nuclear envelope and lamina, as can also be seen in the EM images (Figure 2). This is due to the chemical composition of the DNA, containing carbon and nitrogen as well as phosphorus from the phosphate backbone. Furthermore, regions of different phosphorus and sulfur concentrations can be distinguished in the nucleolus, which

points to the different components, the pars granulosa or granular component (GC) and the pars fibrosa, which is composed of the fibrillar center (FC) and the dense fibrillar component (DFC) [106, 107]. In the FC, transcription of rDNA occurs, leading to an accumulation of phosphorus-rich DNA and RNA [108]. In contrast, the DFC and GC have a high protein content due to the fibrillarin, nucleophosmin and pre-ribosomal protein subunits [109], which can lead to an enrichment of the sulfur content due to thiol side chains of the amino acids, cysteine and methionine. With comparable $^{12}C^{14}N^-$ count rates and strongly detached from the surrounding cytoplasm as well as from the empty area of the enveloping vesicular structure, the *Salmonella* cells stand out in the phagosome (Figure 3 A_1 & B_1). Due the compact cell shape of a bacterium, the phosphorus content is even higher here compared to the nucleolus and the nuclear envelope of macrophages (Figure 3 A_2 & B_2). Thus, phagocytosed bacteria, with a size of 1-2 µm, can be clearly distinguished from the eukaryotic cell structures in shape and size as well as element composition. In addition, mitochondrial structures with a size of around 0.5 µm are characterized by an increased sulfur content, a very low phosphorus content and high $^{12}C^{14}N^-$ count rates [110, 111]. This indicates an increased protein and low nucleic acid content (Figure 3 A_3 & C_1, C_2, C_3).

The O^- ion source was used to analyze the metal distribution where sodium (Na) and calcium (Ca) were preferred for detailed imaging of the whole cell morphology [112]. A preliminary investigation of the samples showed that Mg had a similar cell distribution than Ca (data not shown). Concerning the trace metals, zinc (Zn) was also excluded based on its low ion yield, which in turn resulted in a lack of sensitivity, and thus no Zn signal was detected in the cells during preliminary sample investigation (data not shown). Thus, the remaining metals were grouped in two sets to be analyzed with the O^- ion source, one including, Na, Ca, Fe and Co and another, Na, K, Mn, Ni and Cu, with Na maintained in each analysis to facilitate the cell localization. Additionally, two different beam currents were used to map the same areas: 1.5 pA

for small probe sizes in order to detect the macronutrients Na, Ca, and K, with a higher spatial resolution between 70 nm (small areas) and 100 nm (big areas), and 25 pA for trace metal detection, resulting in larger probe sizes and thus a lower spatial resolution between 120 nm (small areas) and 250 nm (big areas) (Figures 4, 5 & Supplementary Figures 1, 3-5).

The high sensitivity to Ca and Na, based on the high NanoSIMS ion yield using the O^- ion source, allows to image elemental distribution and resolve cell shape and structure of large eukaryotic cells, such as the macrophage cell line used here, as well as subcellular compartments and the *Sa* in the phagosomes. It is possible to visualize large cells in a larger image (up to 65 µm × 65 µm) as well as very small cell components or bacteria, with a high spatial resolution of 70 nm, and to track simultaneously the enrichments of these two macro elements (Figures 4 & 5). Increased calcium accumulation occurs in the areas of the nuclear envelope, the heterochromatin condensation areas and partially in the nucleolus in comparison to the cytosol (Figure 4 B_1 & B_2; Figure 5 & Supplementary Figures 3-5). In the function of calcium in signal transduction, the nuclear envelope serves as a source for nuclear Ca^{2+} waves that turn on gene expression required for adaptive responses [113]. The construction of the core envelope from the inner nuclear membrane (INM) and the outer nuclear membrane (ONM) creates the perinuclear space as intracellular Ca^{2+} storage. The nuclear pore complex (NPC) connects INM with OPNM and enables the separation to the nucleoplasm [114]. Eukaryotic cells use different mechanisms to keep the cytosolic calcium concentration very low. For example, sarcoendoplasmic reticulum calcium ATPase (SERCA), localized in the endoplasmic reticulum (ER) membrane, is used to eliminate calcium from the cytoplasm, as well as the plasma membrane calcium ATPases and sodium–calcium exchangers (NCXs) [115]. This creates a calcium gradient at the membranes and leads here to the differentiation of calcium-enriched subcellular structures (Figure 4 B_1 & B_2). Likewise, the bacterial cells (*Salmonella*) stand out due to an increased calcium but also sodium concentration (Figure 4 A_3 & B_3). It

should be mentioned, that NanoSIMS is extremely sensitive to calcium, even if it is present only in trace amounts, resulting in bright Ca images (Figure 4). This is based on the high secondary ion yield of calcium in NanoSIMS using the oxygen primary ion source and high local Ca concentrations such as in the nuclear envelope. However, these measured intensities do not reflect the Ca quantity compared to other elements.

The greatest challenge for all analytical methods available today, however, lies in the detection of trace elements under non-artificial enrichment. Techniques based on synchrotron X-ray fluorescence (SXRF), scanning x-ray fluorescence microscope (SXFM), Energy-dispersive X-ray spectroscopy (EDS) or mass spectrometry (NanoSIMS and LA-ICP-MS) often reach the limits of detection and spatial resolution in order to visualize these element distributions in detail on a subcellular level [116, 117]. By use of the NanoSIMS 50L in combination with the new Hyperion RF plasma O^- ion source, it is possible to detect normal cell physiological enrichment of trace elements such as Mn, Ni, Cu and Co in individual compartments of the eukaryotic cell as well as bacterial cells with a stand-alone resolution down to 70 nm in this work.

Figure 4 C_3, D_3 & E_3 shows that there is an increased concentration of Mn, Ni and Cu in the *Sa* cells compared to the surrounding cytoplasm of the phagosome of the macrophage cell (Figure 5 & Supplementary Figure 4). Thus, a smaller number of atoms per cell (Figure 1, Supplementary Table 1) due to a much smaller cell volume of the bacteria leads to a concentration increase in this area compared to the distribution and compartmentalization in the eukaryotic cell. Iron and manganese, on the other hand, occurs in macrophage cells with a relatively even distribution (Figure 5).

Unlike all other detectable trace elements, cobalt appears to accumulate in the areas of the nucleus envelope. It is striking that calcium and cobalt show a coincidence in their spatial localization (Figure 5 & Supplementary Figures 4 & 5). The reasons for this are unclear.

However, cobalt accumulation in the area of the cell nucleus and in perinuclear structures was also shown in human HaCaT cells (keratinocytes) during intoxication with high micromolar Co concentrations [118]. The mapping also points to an accumulation of cobalt in the ER, Golgi apparatus or in the perinuclear space. Furthermore, cobalt accumulation can be shown in the bacterial cells. This agrees with a higher percentage ratio of cobalt amounts in the small-volume bacterial cells compared to the eukaryotic cell (Figure 1 & Supplementary Table 1). The biological relevance of cobalt is given in the bacterial cobalamin biosynthesis as well as the eukaryotic use of the resulting vitamin B12 precursors [119, 120]. However, this only gives an indication of the biological relevance but not of the cellular distribution in the prokaryotic cells.

Conclusion

Using the NanoSIMS 50L in combination with the novel Hyperion RF plasma O^- primary ion source, several trace elements can be mapped in cells such as eukaryotic macrophages and small prokaryotic *Salmonella* cells during phagocytosis at the cellular and subcellular level. In particular, the accumulation of cobalt in the nuclear envelope respectively at the nuclear lamina indicates an interesting but still unknown distribution of this trace element in murine macrophages. In addition, an enrichment of copper and nickel could be detected at region of prokaryotic cells. Furthermore, the Cs^+ ion source allows high spatial resolution mapping of cell morphology at subcellular level. In this way, the relevant metal macro- and trace elements detected by the O^- ion source can be assigned to their biological use through allocation to cellular structures and compounds.

Declaration of competing interest

The authors declare that they have no known competing financial interests or personal relationships that could have appeared to influence the work reported in this paper.

Acknowledgements

The work was supported by the project ANR-11-EQPX-0027 MARSS, and by the project 44690PA of the bilateral (German-French) DAAD - Campus France program PROCOPE from the German ‘Bundesministerium für Bildung und Forschung (BMBF)’, the French ‘Ministère de l'Europe et des Affaires étrangères (MEAE)’ and ‘Ministère de l'Enseignement supérieur, de la Recherche et de l'Innovation (MESRI). We also acknowledge to the DFG for providing the ICP-MS by DFG grant INST 271/266-1 to the Martin-Luther-University Halle-Wittenberg and Dietrich H. Nies for laboratory space provision.

Data Availability Statements

The data underlying this article are available in the article and in its online supplementary material.

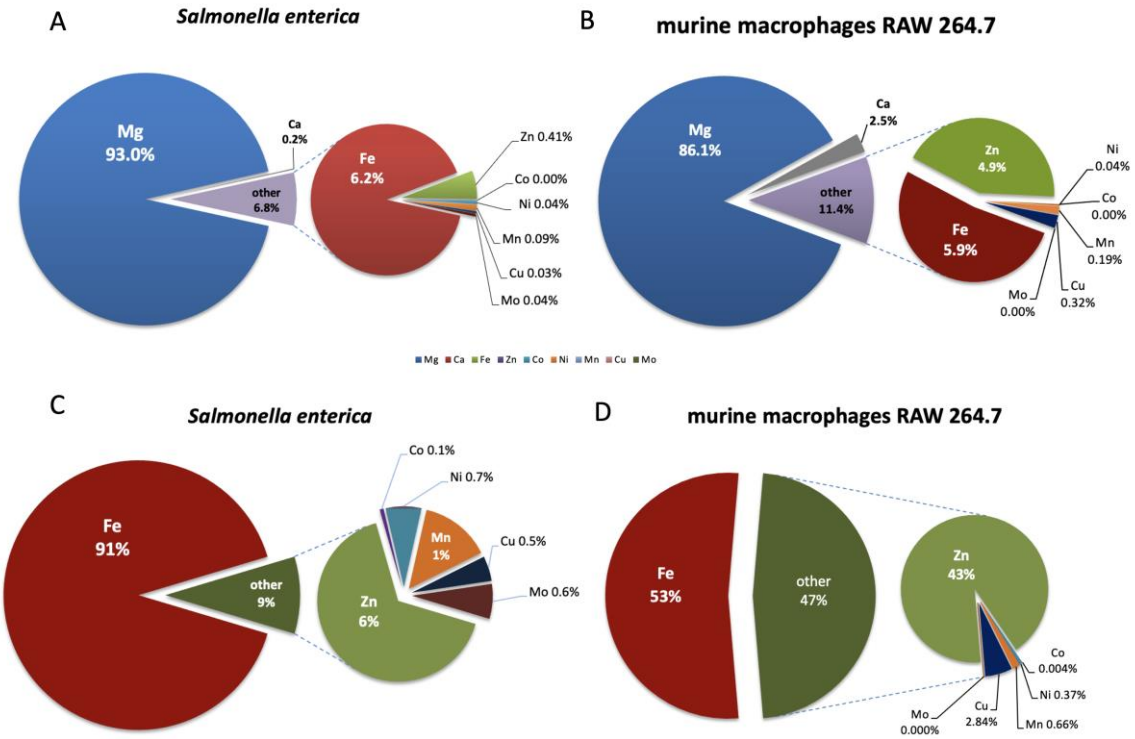

Figure 1 - Cellular metal content ratios of *Salmonella enterica* Serovar Enteritidis and murine macrophage cell line RAW 264.7. Cellular metal content ratios of *Sa* (A & C) and RAW 264.7 (B & D) was measured by ICP-MS and given as percentage ratios (metal quota). The sum of all elements (Mg – magnesium, Fe – iron, Zn – zinc, Co – cobalt, Ni – nickel, Mn – manganese, Cu – copper and Mo – molybdenum) displayed was set to 100% for normalization and the individual percentage was calculated in A & B and the magnesium and calcium content were excluded in C & D.

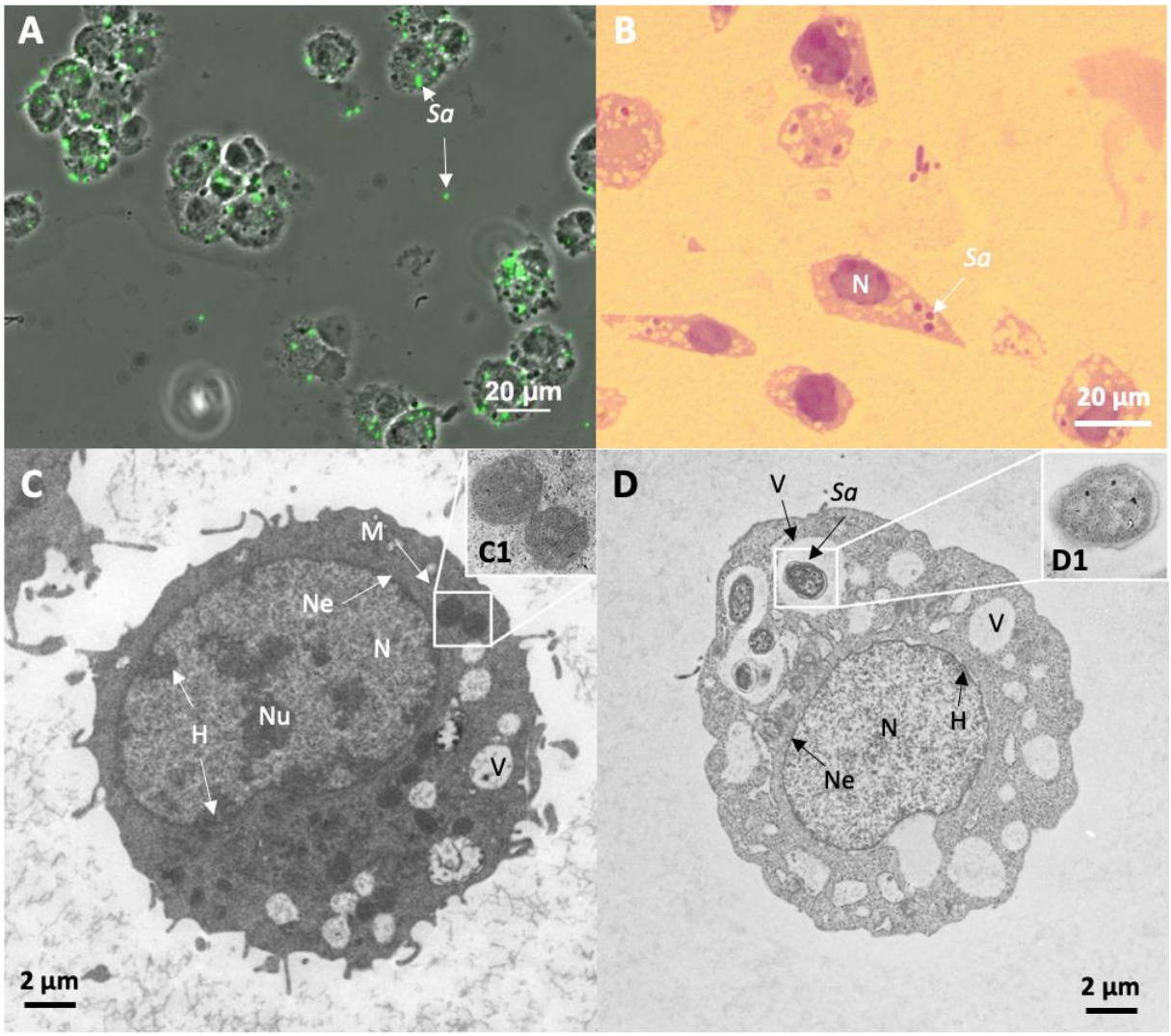

Figure 2 - Morphology of *Salmonella enterica* Serovar Enteritidis (*Sa*) and murine macrophage cell line RAW 264.7 during phagocytosis. A) Merged bright field and fluorescence light microscope image of FITC-marked heat inactivated *Sa* with macrophages, B) Toluidine blue stained semithin section of macrophages co-cultured with vital *Sa*, C) TEM images of a macrophage co-cultured with inactivated bacteria, mitochondria (C1) and D) with vital bacteria like B, *Sa* (D1). *Salmonella* (*Sa*), mitochondria (M), nucleus (N), nucleolus (Nu), nuclear envelope (Ne), vesicle / phagosome (V) and heterochromatin (H).

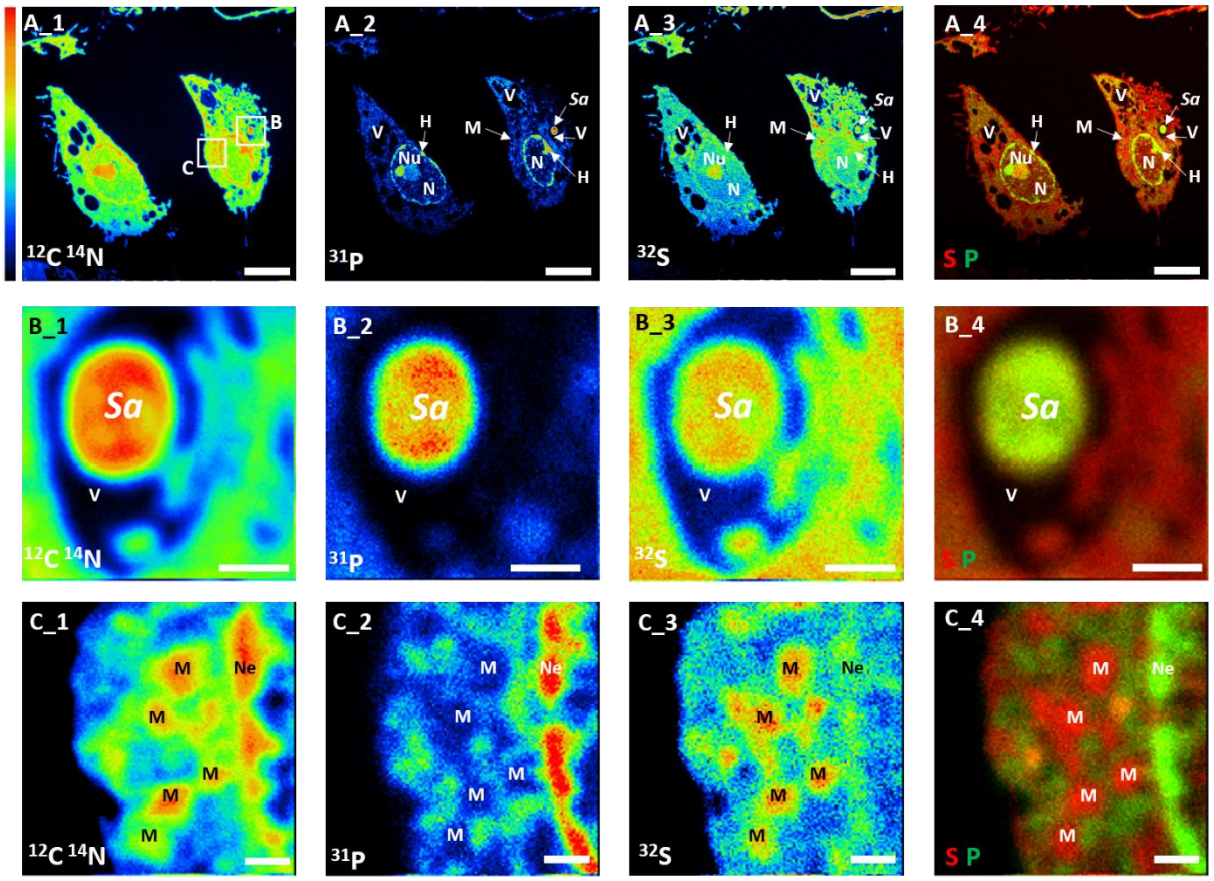

496

497 **Figure 3 - Mapping** of 1) $^{12}C^{14}N^-$, 2) $^{31}P^-$ and 3) $^{32}S^-$ with Cs^+ ions and 4) color overlay of ^{31}P
498 and ^{32}S, of A) two macrophages, and detailed mapping in two regions of interest on the cells,
499 marked with a white square on the first image, showing B) a *Sa* cell inside a phagosome and C)
500 ribosomes and nuclear envelope inside the macrophage cell. Color scale on the top left gives
501 relative intensities of the isotopes count rates. Scale bar: A) 5 µm, B) 0.5 µm, C) 0.5 µm.
502 *Salmonella* (*Sa*), mitochondria (M), nucleus (N), nucleolus (Nu), nuclear envelope (Ne),
503 vesicle/ phagosome (V).

504

505

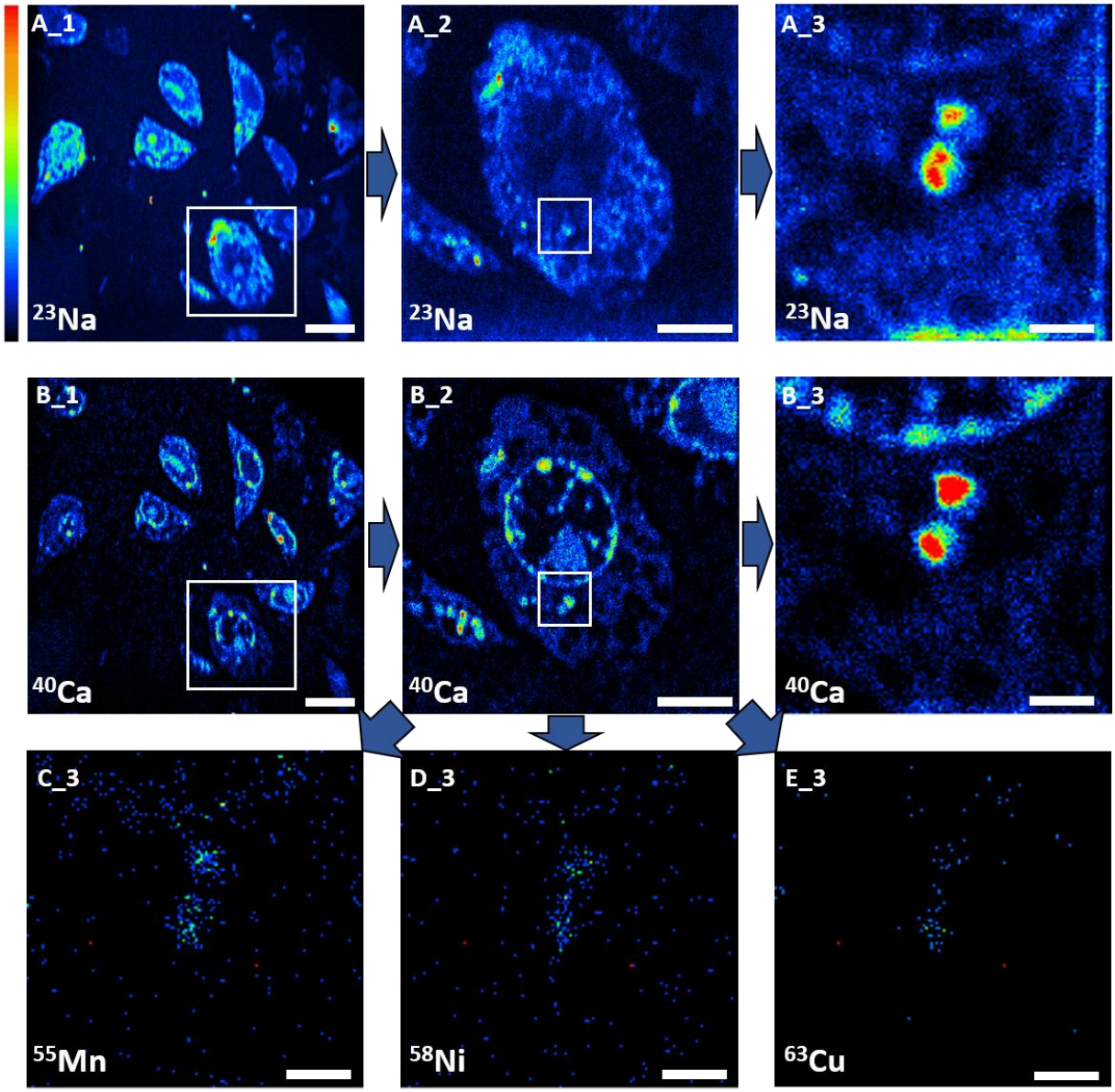

Figure 4 - Mapping of A) $^{23}Na^+$, B) $^{40}Ca^+$, C) $^{55}Mn^+$, D) $^{58}N^+$ and E) $^{63}Cu^+$ with O^- ions of 1) several macrophages, 2) mapping of a selected macrophage (marked in 1 with a white square) and 3) mapping of two *Sa* cells inside a phagosome (marked in 2 with a white square) with high resolution for $^{23}Na^+$ and $^{40}Ca^+$ (A_3 and B_3) and low resolution for $^{55}Mn^+$, $^{58}Ni^+$ and $^{63}Cu^+$ (C_3, D_3 and E_3). Color scale on the top left gives relative intensities of the isotopes count rates. Scale bar: 1) 10 µm, 2) 5 µm, 3) 1 µm.

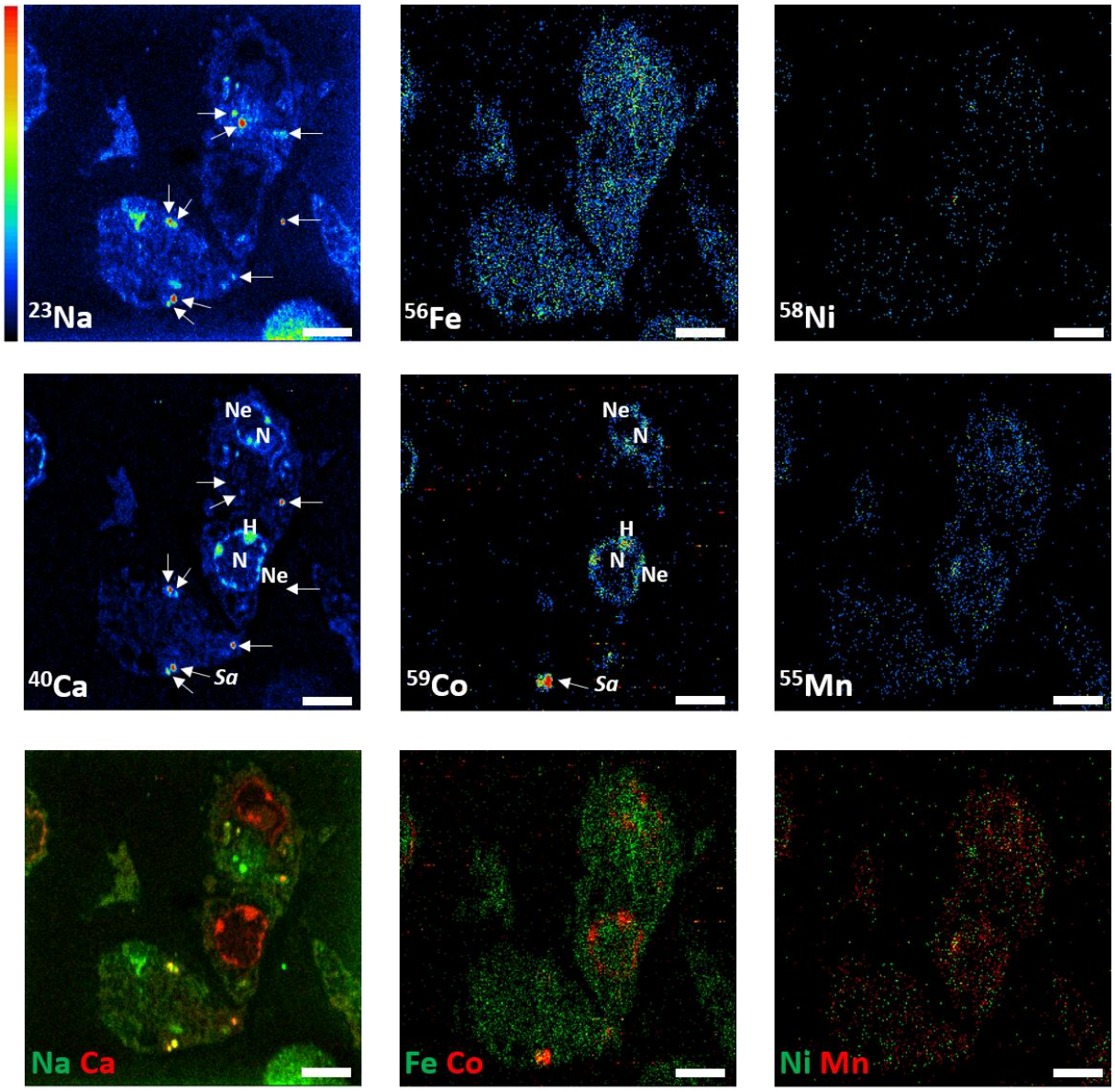

Figure 5 - Mapping of $^{23}Na^{+}$, $^{40}Ca^{+}$, $^{55}Mn^{+}$, $^{56}Fe^{+}$, $^{58}Ni^{+}$ and $^{59}Co^{+}$ with O^{-} ions of three macrophages, and colour overlay of two elements, with *Salmonella* (*Sa*) marked with white arrows on Na^{+} and Ca^{+}, nucleus (N), heterochromatin (H) and nuclear envelope (Ne). Color scale on the top left gives relative intensities of the isotopes count rates. Scale bar: 5 µm.

References

1. Anbar AD, Knoll AH. Proterozoic ocean chemistry and evolution: a bioinorganic bridge? *Science* 2002;**297**(5584):1137-42. doi: 10.1126/science.1069651
2. Knoll AH, Javaux EJ, Hewitt D *et al.* Eukaryotic organisms in Proterozoic oceans. *Philosophical Transactions of the Royal Society B: Biological Sciences* 2006;**361**(1470):1023-38. doi: 10.1098/rstb.2006.1843
3. Ruiz-Trillo I, Burger G, Holland PW *et al.* The origins of multicellularity: a multi-taxon genome initiative. *Trends Genet* 2007;**23**(3):113-8. doi: 10.1016/j.tig.2007.01.005
4. Donoghue PC, Antcliffe JB. Early life: Origins of multicellularity. *Nature* 2010;**466**(7302):41-2. doi: 10.1038/466041a
5. Niklas KJ. The evolutionary-developmental origins of multicellularity. *Am J Bot* 2014;**101**(1):6-25. doi: 10.3732/ajb.1300314
6. Hao X, Luthje F, Ronn R *et al.* A role for copper in protozoan grazing - two billion years selecting for bacterial copper resistance. *Mol Microbiol* 2016;**102**(4):628-41. doi: 10.1111/mmi.13483
7. Hood MI, Skaar EP. Nutritional immunity: transition metals at the pathogen-host interface. *Nature Reviews Microbiology* 2012;**10**(8):525-37. doi: 10.1038/nrmicro2836
8. Chandrangsu P, Rensing C, Helmann JD. Metal homeostasis and resistance in bacteria. *Nat Rev Microbiol* 2017;**15**(6):338-50. doi: 10.1038/nrmicro.2017.15
9. Hao XL, Luthje FL, Qin Y *et al.* Survival in amoeba-a major selection pressure on the presence of bacterial copper and zinc resistance determinants? Identification of a "copper pathogenicity island". *Applied Microbiology and Biotechnology* 2015;**99**(14):5817-24. doi: 10.1007/s00253-015-6749-0
10. Capdevila DA, Wang J, Giedroc DP. Bacterial Strategies to Maintain Zinc Metallostasis at the Host-Pathogen Interface. *J Biol Chem* 2016;**291**(40):20858-68. doi: 10.1074/jbc.R116.742023
11. Buracco S, Peracino B, Andreini C *et al.* Differential Effects of Iron, Zinc, and Copper on *Dictyostelium discoideum* Cell Growth and Resistance to L*egionella pneumophila*. *Front Cell Infect Microbiol* 2017;**7**:536. doi: 10.3389/fcimb.2017.00536
12. Soldati T, Neyrolles O. Mycobacteria and the intraphagosomal environment: take it with a pinch of salt(s)! *Traffic* 2012;**13**(8):1042-52. doi: 10.1111/j.1600-0854.2012.01358.x
13. Botella H, Stadthagen G, Lugo-Villarino G *et al.* Metallobiology of host-pathogen interactions: an intoxicating new insight. *Trends Microbiol* 2012;**20**(3):106-12. doi: 10.1016/j.tim.2012.01.005
14. Schaumlöffel D, Hutchinson R, Malherbe J *et al.* Novel Methods for Bioimaging Including LA-ICP-MS, NanoSIMS, TEM/X-EDS, and SXRF. *Metallomics*, 2016, 83-116
15. Nunez J, Renslow R, Cliff JB *et al.* NanoSIMS for biological applications: Current practices and analyses. *Biointerphases* 2018;**13**(3). doi: Artn 03b301 10.1116/1.4993628
16. Lechene C, Hillion F, McMahon G *et al.* High-resolution quantitative imaging of mammalian and bacterial cells using stable isotope mass spectrometry. *J Biol* 2006;**5**(6):20. doi: 10.1186/jbiol42
17. MacDonald RJ. Surface Analysis Methods in Materials Science. In: O'Connor J, Sexton, Brett, Smart, Roger S.C.s (ed), 2003
18. Malherbe J, Penen F, Isaure MP *et al.* A New Radio Frequency Plasma Oxygen Primary Ion Source on Nano Secondary Ion Mass Spectrometry for Improved Lateral Resolution and Detection of Electropositive Elements at Single Cell Level. *Anal Chem* 2016;**88**(14):7130-6. doi: 10.1021/acs.analchem.6b01153
19. Gao D, Huang X, Tao Y. A critical review of NanoSIMS in analysis of microbial metabolic activities at single-cell level. *Crit Rev Biotechnol* 2016;**36**(5):884-90. doi: 10.3109/07388551.2015.1057550
20. Chadwick GL, Otero FJ, Gralnick JA *et al.* NanoSIMS imaging reveals metabolic stratification within current-producing biofilms. *Proc Natl Acad Sci U S A* 2019;**116**(41):20716-24. doi: 10.1073/pnas.1912498116

21. Fayek M, Utsunomiya S, Pfiffner SM *et al.* The application of HRTEM techniques and nanosims to chemically and isotopically characterize *Geobacter sulfurreducens* surfaces. *Can Mineral* 2005;**43**:1631-41. doi: DOI 10.2113/gscanmin.43.5.1631
22. Newsome L, Adams RL, Downie HF *et al.* NanoSIMS imaging of extracellular electron transport processes during microbial iron(III) reduction. *FEMS Microbiol Ecol* 2018;**94**(8). doi: ARTN fiy104 10.1093/femsec/fiy104
23. Iarovaia OV, Minina EP, Sheval EV *et al.* Nucleolus: A Central Hub for Nuclear Functions. *Trends Cell Biol* 2019;**29**(8):647-59. doi: 10.1016/j.tcb.2019.04.003
24. Fleming EJ, Woyke T, Donatello RA *et al.* Insights into the Fundamental Physiology of the Uncultured Fe-Oxidizing Bacterium *Leptothrix ochracea*. *Applied and Environmental Microbiology* 2018;**84**(9). doi: ARTN e02239-17 10.1128/AEM.02239-17
25. Du HH, Huang QY, Zhou M *et al.* Sorption of Cu(II) by Al hydroxide organo-mineral coprecipitates: Microcalorimetry and NanoSIMS observations. *Chem Geol* 2018;**499**:165-71. doi: 10.1016/j.chemgeo.2018.09.026
26. Lopez-Adams R, Newsome L, Moore KL *et al.* Dissimilatory Fe(III) Reduction Controls on Arsenic Mobilization: A Combined Biogeochemical and NanoSIMS Imaging Approach. *Front Microbiol* 2021;**12**. doi: ARTN 640734 10.3389/fmicb.2021.640734
27. Ferrari A, He C, Kennelly JP *et al.* Aster Proteins Regulate the Accessible Cholesterol Pool in the Plasma Membrane. *Mol Cell Biol* 2020;**40**(19). doi: 10.1128/MCB.00255-20
28. Hu X, Weston TA, He C *et al.* Release of cholesterol-rich particles from the macrophage plasma membrane during movement of filopodia and lamellipodia. *Elife* 2019;**8**. doi: 10.7554/eLife.50231
29. He CW, Migawa MT, Chen K *et al.* High-resolution visualization and quantification of nucleic acid-based therapeutics in cells and tissues using Nanoscale secondary ion mass spectrometry (NanoSIMS). *Nucleic Acids Res* 2021;**49**(1):1-14. doi: 10.1093/nar/gkaa1112
30. Fearns A, Greenwood DJ, Rodgers A *et al.* Correlative light electron ion microscopy reveals in vivo localisation of bedaquiline in *Mycobacterium tuberculosis*-infected lungs. *PLoS Biol* 2020;**18**(12). doi: ARTN e3000879 10.1371/journal.pbio.3000879
31. Jiang HB, Passarelli MK, Munro PMG *et al.* High-resolution sub-cellular imaging by correlative NanoSIMS and electron microscopy of amiodarone internalisation by lung macrophages as evidence for drug-induced phospholipidosis. *Chem Commun* 2017;**53**(9):1506-9. doi: 10.1039/c6cc08549k
32. Kitamura N, Ektessabi AM. XAFS in a single macrophage cell. *J Synchrotron Radiat* 2001;**8**(Pt 2):981-3. doi: 10.1107/s0909049500014436
33. Ishihara R, Ide-Ektessabi A, Kitamura N *et al.* Investigation of interactions of nano-particles within cells using micro-beam imaging techniques. *X-Ray Spectrom* 2003;**32**(6):418-22. doi: 10.1002/xrs.663
34. Barst BD, Bridges K, Korbas M *et al.* The role of melano-macrophage aggregates in the storage of mercury and other metals: an example from yelloweye rockfish (*Sebastes ruberrimus*). *Environ Toxicol Chem* 2015;**34**(8):1918-25. doi: 10.1002/etc.3009
35. Pascolo L, Gianoncelli A, Schneider G *et al.* The interaction of asbestos and iron in lung tissue revealed by synchrotron-based scanning X-ray microscopy. *Sci Rep* 2013;**3**:1123. doi: 10.1038/srep01123
36. Bussy C, Paineau E, Cambedouzou J *et al.* Intracellular fate of carbon nanotubes inside murine macrophages: pH-dependent detachment of iron catalyst nanoparticles. *Part Fibre Toxicol* 2013;**10**. doi: Artn 24 10.1186/1743-8977-10-24
37. Liang-Takasaki CJ, Makela PH, Leive L. Phagocytosis of bacteria by macrophages: changing the carbohydrate of lipopolysaccharide alters interaction with complement and macrophages. *J Immunol* 1982;**128**(3):1229-35

38. Muniz-Junqueira MI, Prata A, Tosta CE. Factors influencing phagocytosis of *Salmonella typhimurium* by macrophages in murine schistosomiasis. *Rev Soc Bras Med Trop* 1997;**30**(2):101-6. doi: 10.1590/s0037-86821997000200003
39. Shi L, Chowdhury SM, Smallwood HS *et al.* Proteomic investigation of the time course responses of RAW 264.7 macrophages to infection with Salmonella enterica. *Infect Immun* 2009;**77**(8):3227-33. doi: 10.1128/IAI.00063-09
40. Hurley D, Hoffmann M, Muruvanda T *et al.* Atypical *Salmonella enterica* Serovars in Murine and Human Macrophage Infection Models. *Infect Immun* 2020;**88**(4). doi: 10.1128/IAI.00353-19
41. Spurr AR. A low-viscosity epoxy resin embedding medium for electron microscopy. *Journal of ultrastructure research* 1969;**26**(1):31-43
42. Waldron KJ, Rutherford JC, Ford D *et al.* Metalloproteins and metal sensing. *Nature* 2009;**460**(7257):823-30. doi: 10.1038/nature08300
43. Foster AW, Osman D, Robinson NJ. Metal preferences and metallation. *J Biol Chem* 2014;**289**(41):28095-103. doi: 10.1074/jbc.R114.588145
44. Juttukonda LJ, Skaar EP. Chapter 31 - Manganese and Nutritional Immunity. In: Collins JFs (ed). *Molecular, Genetic, and Nutritional Aspects of Major and Trace Minerals*. Boston: Academic Press, 2017, 377-87
45. Spears JW, Engle TE. Feed Ingredients: Feed Supplements: Microminerals. *Reference Module in Food Science*: Elsevier, 2016
46. Festa RA, Thiele DJ. Copper at the Front Line of the Host-Pathogen Battle. *Plos Pathogens* 2012;**8**(9):e1002887. doi: ARTN e1002887
10.1371/journal.ppat.1002887
47. Kim BE, Nevitt T, Thiele DJ. Mechanisms for copper acquisition, distribution and regulation. *Nat Chem Biol* 2008;**4**(3):176-85. doi: 10.1038/nchembio.72
48. Thorgersen MP, Downs DM. Cobalt targets multiple metabolic processes in *Salmonella enterica*. *J Bacteriol* 2007;**189**(21):7774-81. doi: 10.1128/JB.00962-07
49. Rodionov DA, Vitreschak AG, Mironov AA *et al.* Comparative genomics of the vitamin B12 metabolism and regulation in prokaryotes. *J Biol Chem* 2003;**278**(42):41148-59. doi: 10.1074/jbc.M305837200
50. Arfin SM, Kendall RL, Hall L *et al.* Eukaryotic methionyl aminopeptidases: two classes of cobalt-dependent enzymes. *Proc Natl Acad Sci U S A* 1995;**92**(17):7714-8. doi: 10.1073/pnas.92.17.7714
51. Alfano M, Cavazza C. Structure, function, and biosynthesis of nickel-dependent enzymes. *Protein Sci* 2020;**29**(5):1071-89. doi: 10.1002/pro.3836
52. Mayr SJ, Mendel RR, Schwarz G. Molybdenum cofactor biology, evolution and deficiency. *Biochim Biophys Acta Mol Cell Res* 2021;**1868**(1):118883. doi: 10.1016/j.bbamcr.2020.118883
53. Mendel RR, Kruse T. Cell biology of molybdenum in plants and humans. *Bba-Mol Cell Res* 2012;**1823**(9):1568-79. doi: 10.1016/j.bbamcr.2012.02.007
54. Watly J, Potocki S, Rowinska-Zyrek M. Zinc Homeostasis at the Bacteria/Host Interface-From Coordination Chemistry to Nutritional Immunity. *Chemistry (Easton)* 2016;**22**(45):15992-6010. doi: 10.1002/chem.201602376
55. Muckenthaler MU, Rivella S, Hentze MW *et al.* A Red Carpet for Iron Metabolism. *Cell* 2017;**168**(3):344-61. doi: 10.1016/j.cell.2016.12.034
56. Gao G, Li J, Zhang Y *et al.* Cellular Iron Metabolism and Regulation. *Adv Exp Med Biol* 2019;**1173**:21-32. doi: 10.1007/978-981-13-9589-5_2
57. Carrondo MA. Ferritins, iron uptake and storage from the bacterioferritin viewpoint. *EMBO J* 2003;**22**(9):1959-68. doi: 10.1093/emboj/cdg215
58. Lane DJ, Merlot AM, Huang ML *et al.* Cellular iron uptake, trafficking and metabolism: Key molecules and mechanisms and their roles in disease. *Biochim Biophys Acta* 2015;**1853**(5):1130-44. doi: 10.1016/j.bbamcr.2015.01.021
59. Hider RC, Maret W. Iron and zinc sensing in cells and the body. *Metallomics* 2015;**7**(2):200-1. doi: 10.1039/c4mt90051k

60. Johnson DC, Dean DR, Smith AD *et al.* Structure, function, and formation of biological iron-sulfur clusters. *Annu Rev Biochem* 2005;**74**:247-81. doi: 10.1146/annurev.biochem.74.082803.133518
61. Prasad AS. Zinc: role in immunity, oxidative stress and chronic inflammation. *Curr Opin Clin Nutr Metab Care* 2009;**12**(6):646-52. doi: 10.1097/MCO.0b013e3283312956
62. Bonaventura P, Benedetti G, Albarede F *et al.* Zinc and its role in immunity and inflammation. *Autoimmun Rev* 2014. doi: 10.1016/j.autrev.2014.11.008
63. Andreini C, Banci L, Bertini I *et al.* Zinc through the three domains of life. *J Proteome Res* 2006;**5**(11):3173-8. doi: Doi 10.1021/Pr0603699
64. Andreini C, Banci L, Bertini I *et al.* Non-heme iron through the three domains of life. *Proteins* 2007;**67**(2):317-24. doi: 10.1002/prot.21324
65. Maret W. Metalloproteomics, metalloproteomes, and the annotation of metalloproteins. *Metallomics* 2010;**2**(2):117-25. doi: 10.1039/b915804a
66. Andreini C, Banci L, Bertini I *et al.* Counting the zinc-proteins encoded in the human genome. *J Proteome Res* 2006;**5**(1):196-201. doi: 10.1021/pr050361j
67. Andreini C, Bertini I, Rosato A. Metalloproteomes: a bioinformatic approach. *Acc Chem Res* 2009;**42**(10):1471-9. doi: 10.1021/ar900015x
68. Dupont CL, Yang S, Palenik B *et al.* Modern proteomes contain putative imprints of ancient shifts in trace metal geochemistry. *Proc Natl Acad Sci U S A* 2006;**103**(47):17822-7. doi: 10.1073/pnas.0605798103
69. Dupont CL, Butcher A, Valas RE *et al.* History of biological metal utilization inferred through phylogenomic analysis of protein structures. *Proc Natl Acad Sci U S A* 2010;**107**(23):10567-72. doi: 10.1073/pnas.0912491107
70. Miloch A, Krezel A. Metal binding properties of the zinc finger metallome - insights into variations in stability. *Metallomics* 2014. doi: 10.1039/c4mt00149d
71. Krezel A, Maret W. Thionein/metallothionein control Zn(II) availability and the activity of enzymes. *J Biol Inorg Chem* 2008;**13**(3):401-9. doi: 10.1007/s00775-007-0330-y
72. Blindauer CA. Bacterial metallothioneins: past, present, and questions for the future. *J Biol Inorg Chem* 2011;**16**(7):1011-24. doi: 10.1007/s00775-011-0790-y
73. Isani G, Carpene E. Metallothioneins, unconventional proteins from unconventional animals: a long journey from nematodes to mammals. *Biomolecules* 2014;**4**(2):435-57. doi: 10.3390/biom4020435
74. Ma Z, Chandrangsu P, Helmann TC *et al.* Bacillithiol is a major buffer of the labile zinc pool in *Bacillus subtilis*. *Mol Microbiol* 2014;**94**(4):756-70. doi: 10.1111/mmi.12794
75. Hensley MP, Tierney DL, Crowder MW. Zn(II) binding to *Escherichia coli* 70S ribosomes. *Biochemistry* 2011;**50**(46):9937-9. doi: 10.1021/bi200619w
76. Chandrangsu P, Huang X, Gaballa A *et al. Bacillus subtilis* FolE is sustained by the ZagA zinc metallochaperone and the alarmone ZTP under conditions of zinc deficiency. *Mol Microbiol* 2019;**112**(3):751-65. doi: 10.1111/mmi.14314
77. Chandrangsu P, Rensing C, Helmann JD. Metal homeostasis and resistance in bacteria. *Nature Reviews Microbiology* 2017;**15**(6):338-50. doi: 10.1038/nrmicro.2017.15
78. Haas CE, Rodionov DA, Kropat J *et al.* A subset of the diverse COG0523 family of putative metal chaperones is linked to zinc homeostasis in all kingdoms of life. *BMC Genomics* 2009;**10**. doi: Artn 470 Doi 10.1186/1471-2164-10-470
79. Campbell AK. *Intracellular Calcium.* Wiley, 2014
80. Clapham DE. Calcium signaling. *Cell* 1995;**80**(2):259-68. doi: 10.1016/0092-8674(95)90408-5
81. Chang CJ. Searching for harmony in transition-metal signaling. *Nat Chem Biol* 2015;**11**(10):744-7. doi: 10.1038/nchembio.1913
82. Dominguez DC, Guragain M, Patrauchan M. Calcium binding proteins and calcium signaling in prokaryotes. *Cell Calcium* 2015;**57**(3):151-65. doi: 10.1016/j.ceca.2014.12.006
83. Dominguez DC. Calcium signalling in bacteria. *Mol Microbiol* 2004;**54**(2):291-7. doi: 10.1111/j.1365-2958.2004.04276.x

84. Asmat TM, Tenenbaum T, Jonsson AB *et al.* Impact of calcium signaling during infection of *Neisseria meningitidis* to human brain microvascular endothelial cells. *PLoS One* 2014;**9**(12):e114474. doi: 10.1371/journal.pone.0114474
85. Hay AJ, Yang M, Xia X *et al.* Calcium Enhances Bile Salt-Dependent Virulence Activation in Vibrio cholerae. *Infect Immun* 2017;**85**(1). doi: 10.1128/IAI.00707-16
86. Gangola P, Rosen BP. Maintenance of intracellular calcium in *Escherichia coli*. *J Biol Chem* 1987;**262**(26):12570-4
87. Knight MR, Campbell AK, Smith SM *et al.* Recombinant Aequorin as a Probe for Cytosolic Free Ca2+ in *Escherichia coli*. *FEBS Lett* 1991;**282**(2):405-8. doi: Doi 10.1016/0014-5793(91)80524-7
88. Jones HE, Holland IB, Baker HL *et al.* Slow changes in cytosolic free Ca2+ in *Escherichia coli* highlight two putative influx mechanisms in response to changes in extracellular calcium. *Cell Calcium* 1999;**25**(3):265-74. doi: DOI 10.1054/ceca.1999.0028
89. Torrecilla I, Leganes F, Bonilla I *et al.* Use of recombinant aequorin to study calcium homeostasis and monitor calcium transients in response to heat and cold shock in cyanobacterial. *Plant Physiol* 2000;**123**(1):161-75. doi: DOI 10.1104/pp.123.1.161
90. Guragain M, Lenaburg DL, Moore FS *et al.* Calcium homeostasis in *Pseudomonas aeruginosa* requires multiple transporters and modulates swarming motility. *Cell Calcium* 2013;**54**(5):350-61. doi: 10.1016/j.ceca.2013.08.004
91. Rabinovitch M. Professional and non-professional phagocytes: an introduction. *Trends Cell Biol* 1995;**5**(3):85-7. doi: 10.1016/s0962-8924(00)88955-2
92. Ambrose CT. The Osler slide, a demonstration of phagocytosis from 1876 Reports of phagocytosis before Metchnikoff's 1880 paper. *Cell Immunol* 2006;**240**(1):1-4. doi: 10.1016/j.cellimm.2006.05.008
93. Gordon S. Phagocytosis: An Immunobiologic Process. *Immunity* 2016;**44**(3):463-75. doi: 10.1016/j.immuni.2016.02.026
94. Tauber AI. Immunity: How Elie Metchnikoff Changed the Course of Modern Medicine. *Bull Hist Med* 2017;**91**(1):140-2. doi: DOI 10.1353/bhm.2017.0015
95. Walters MN, Papadimitriou JM. Phagocytosis: a review. *CRC Crit Rev Toxicol* 1978;**5**(4):377-421. doi: 10.3109/10408447809081012
96. Aderem A, Underhill DM. Mechanisms of phagocytosis in macrophages. *Annu Rev Immunol* 1999;**17**:593-623. doi: 10.1146/annurev.immunol.17.1.593
97. Rosales C, Uribe-Querol E. Phagocytosis: A Fundamental Process in Immunity. *Biomed Res Int* 2017;**2017**:9042851. doi: 10.1155/2017/9042851
98. Kirsten A, Herzberg M, Voigt A *et al.* Contributions of five secondary metal uptake systems to metal homeostasis of *Cupriavidus metallidurans* CH34. *J Bacteriol* 2011;**193**(18):4652-63. doi: 10.1128/JB.05293-11
99. Biology and brimstone. *Nat Chem Biol* 2006;**2**(4):169. doi: 10.1038/nchembio0406-169
100. Fernandez-Garcia C, Coggins AJ, Powner MW. A Chemist's Perspective on the Role of Phosphorus at the Origins of Life. *Life-Basel* 2017;**7**(3). doi: ARTN 31 10.3390/life7030031
101. Gross M. Where is all the phosphorus? *Curr Biol* 2017;**27**(21):R1141-R4
102. Fagerbakke KM, Heldal M, Norland S. Content of carbon, nitrogen, oxygen, sulfur and phosphorus in native aquatic and cultured bacteria. *Aquat Microb Ecol* 1996;**10**(1):15-27. doi: DOI 10.3354/ame010015
103. Vrede K, Heldal M, Norland S *et al.* Elemental composition (C, N, P) and cell volume of exponentially growing and nutrient-limited bacterioplankton. *Appl Environ Microbiol* 2002;**68**(6):2965-71. doi: 10.1128/aem.68.6.2965-2971.2002
104. Xu X, Hui D, King AW *et al.* Convergence of microbial assimilations of soil carbon, nitrogen, phosphorus, and sulfur in terrestrial ecosystems. *Sci Rep* 2015;**5**:17445. doi: 10.1038/srep17445
105. Storms HA, Brown KF, Stein JD. Evaluation of a Cesium Positive-Ion Source for Secondary Ion Mass-Spectrometry. *Anal Chem* 1977;**49**(13):2023-30. doi: DOI 10.1021/ac50021a034

106. Hernandez-Verdun D, Roussel P, Thiry M *et al.* The nucleolus: structure/function relationship in RNA metabolism. *Wires Rna* 2010;**1**(3):415-31. doi: 10.1002/wrna.39
107. O'Sullivan JM, Pai DA, Cridge AG *et al.* The nucleolus: a raft adrift in the nuclear sea or the keystone in nuclear structure? *Biomol Concepts* 2013;**4**(3):277-86. doi: 10.1515/bmc-2012-0043
108. Sirri V, Urcuqui-Inchima S, Roussel P *et al.* Nucleolus: the fascinating nuclear body. *Histochem Cell Biol* 2008;**129**(1):13-31. doi: 10.1007/s00418-007-0359-6
109. Raska I, Shaw PJ, Cmarko D. Structure and function of the nucleolus in the spotlight. *Curr Opin Cell Biol* 2006;**18**(3):325-34. doi: 10.1016/j.ceb.2006.04.008
110. Gupta A, Becker T. Mechanisms and pathways of mitochondrial outer membrane protein biogenesis. *Bba-Bioenergetics* 2021;**1862**(1). doi: ARTN 148323
10.1016/j.bbabio.2020.148323
111. Becker T, Gebert M, Pfanner N *et al.* Biogenesis of mitochondrial membrane proteins. *Curr Opin Cell Biol* 2009;**21**(4):484-93. doi: 10.1016/j.ceb.2009.04.002
112. Wilson RG, Stevie FA, Magee CW. *Secondary ion mass spectrometry : a practical handbook for depth profiling and bulk impurity analysis / R. G. Wilson, F. A. Stevie, C. W. Magee.* New York: Wiley, 1989
113. Samer S, Raman R, Laube G *et al.* The nuclear lamina is a hub for the nuclear function of Jacob. *Mol Brain* 2021;**14**(1). doi: ARTN 9
10.1186/s13041-020-00722-1
114. Secondo A, Petrozziello T, Tedeschi V *et al.* Nuclear localization of NCX: Role in Ca(2+) handling and pathophysiological implications. *Cell Calcium* 2020;**86**:102143. doi: 10.1016/j.ceca.2019.102143
115. Bading H. Nuclear calcium signalling in the regulation of brain function. *Nature Reviews Neuroscience* 2013;**14**(9):593-608. doi: 10.1038/nrn3531
116. Kashiv Y, Austin JR, 2nd, Lai B *et al.* Imaging trace element distributions in single organelles and subcellular features. *Sci Rep* 2016;**6**:21437. doi: 10.1038/srep21437
117. Matsuyama S, Shimura M, Mirnura H *et al.* Trace element mapping of a single cell using a hard x-ray nanobeam focused by a Kirkpatrick-Baez mirror system. *X-Ray Spectrom* 2009;**38**(2):89-94. doi: 10.1002/xrs.1123
118. Ortega R, Bresson C, Fraysse A *et al.* Cobalt distribution in keratinocyte cells indicates nuclear and perinuclear accumulation and interaction with magnesium and zinc homeostasis. *Toxicol Lett* 2009;**188**(1):26-32. doi: 10.1016/j.toxlet.2009.02.024
119. Banerjee R. B12 trafficking in mammals: A for coenzyme escort service. *ACS Chem Biol* 2006;**1**(3):149-59. doi: 10.1021/cb6001174
120. Yamada K. Cobalt: its role in health and disease. *Met Ions Life Sci* 2013;**13**:295-320. doi: 10.1007/978-94-007-7500-8_9